AGU PUBLICATIONS

Geochemistry, Geophysics, Geosystems

RESEARCH ARTICLE

10.1002/2015GC005973

Key Points:
- Fracture permeability in ultramafic rocks decreases rapidly as a result of serpentinization
- Serpentinization can rapidly seal permeability in ultramafic-hosted hydrothermal systems
- Generation of new permeability is required to maintain ultramafic-hosted hydrothermal systems

Supporting Information:
- Supporting Information S1

Correspondence to:
A. Farough,
afarough@vt.edu

Citation:
Farough, A., D. E. Moore, D. A. Lockner, and R. P. Lowell (2016), Evolution of fracture permeability of ultramafic rocks undergoing serpentinization at hydrothermal conditions: An experimental study, *Geochem. Geophys. Geosyst.*, *17*, 44–55, doi:10.1002/2015GC005973.

Received 7 JUL 2015
Accepted 7 DEC 2015
Accepted article online 14 DEC 2015
Published online 9 JAN 2016

Evolution of fracture permeability of ultramafic rocks undergoing serpentinization at hydrothermal conditions: An experimental study

A. Farough[1], D. E. Moore[2], D. A. Lockner[2], and R. P. Lowell[1]

[1]Department of Geosciences, Virginia Tech, Blacksburg, Virginia, USA, [2]U.S. Geological Survey, Menlo Park, California, USA

Abstract We performed flow-through laboratory experiments on five cylindrically cored samples of ultramafic rocks, in which we generated a well-mated through-going tensile fracture, to investigate evolution of fracture permeability during serpentinization. The samples were tested in a triaxial loading machine at a confining pressure of 50 MPa, pore pressure of 20 MPa, and temperature of 260°C, simulating a depth of 2 km under hydrostatic conditions. A pore pressure difference of up to 2 MPa was imposed across the ends of the sample. Fracture permeability decreased by 1–2 orders of magnitude during the 200–330 h experiments. Electron microprobe and SEM data indicated the formation of needle-shaped crystals of serpentine composition along the walls of the fracture, and chemical analyses of sampled pore fluids were consistent with dissolution of ferro-magnesian minerals. By comparing the difference between fracture permeability and matrix permeability measured on intact samples of the same rock types, we concluded that the contribution of the low matrix permeability to flow is negligible and essentially all of the flow is focused in the tensile fracture. The experimental results suggest that the fracture network in long-lived hydrothermal circulation systems can be sealed rapidly as a result of mineral precipitation, and generation of new permeability resulting from a combination of tectonic and crystallization-induced stresses is required to maintain fluid circulation.

1. Introduction

The permeability of fractured rocks and its temporal evolution are of critical importance for understanding hydrothermal processes in oceanic crust near and away from oceanic spreading centers. At many of the high-temperature hydrothermal systems located on slow and ultraslow spreading ridges, such as Rainbow and Logatchev vent fields on the Mid-Atlantic Ridge (MAR) [e.g., *Batuyev et al*., 1994; *Bogdanov et al*., 1995; *Charlou et al*., 2002], and on Southwest Indian Ridge [*Bach et al*., 2002], fluids are transported in part through ultramafic rocks. The Lost City Hydrothermal Field located on 1.5 Ma crust on the Atlantis Massif (AM) [e.g., *Kelley et al*., 2001], and the recently discovered Von Damm Hydrothermal Field near the Mid-Cayman Spreading Center [*Connelly et al*., 2012], represent a class of off-axis circulation systems that emanate fluids at low temperatures. The permeability required to allow such vigorous circulation is estimated to be $\sim 10^{-12}-10^{-14}$ m^2 [e.g., *Lowell et al*., 2013], indicating that permeability is governed by faults and fractures.

As fluid circulates through fractures in ultramafic rocks, it promotes a set of hydration reactions in the host rock, commonly referred to as serpentinization, plays an important role in the structure of oceanic crust [e.g., *Cann et al*., 1997; *Escartin et al*., 2001]. During serpentinization, olivine and pyroxene are replaced by serpentine, magnetite, brucite, talc, and carbonate minerals, thus altering the chemical, mechanical, magnetic, seismic, and hydraulic properties of the crust [e.g., *Carlson*, 2001; *Cannat*, 1993]. A key feature of these reactions is volume expansion [e.g., *Coleman*, 1971; *O'Hanley*, 1992], which tends to reduce porosity and permeability and inhibit fluid circulation. Thus, it seems intuitive that serpentinization reactions will tend to be self-limiting; however, hydrothermal systems hosted in extensively serpentinized ultramafic rocks remain active for thousands of years [e.g., *Früh-Green et al*., 2003]. Fracturing and pervasive alteration have been observed in many IODP samples and ophiolitic complexes [e.g., *Beard et al*., 2009; *Kelemen and Hirth*, 2012; *Plümper et al*., 2012]. It is therefore of considerable importance to understand the evolution of permeability in fractured ultramafic rocks.

Previous experimental studies of fault-rock behavior under hydrothermal conditions did not always include permeability measurements [e.g., *Karner et al*., 1997; *Nakatani*, 1998]. *Moore et al*. [1994] measured the matrix permeability of Westerly granite in the temperature range 300–500°C at 50 MPa effective pressure, simulating temperature conditions near the base of the seismogenic zone. They found that reduction in permeability and healing and sealing of microfractures resulted from introduction of hydrothermal fluids to heated granite samples. *Evans et al*. [1997] compared the permeability of fault rocks with that of the undeformed granitic host rock and concluded that fluid-rock reactions strongly affect the permeability structure of fault zones. *Olsen et al*. [1998] observed permeability cycling during deformation experiments at elevated temperatures resulting from the formation and breaking of mineral seals. *Tenthorey et al*. [1998] and *Aharonov et al*. [1998] related permeability decreases to authigenic mineral formation during diagenesis experiments at elevated temperatures on labradorite/quartz sand. *Polak et al*. [2003] studied the rate of aperture reduction in a natural fracture of a novaculite as a result of mineral dissolution and precipitation.

There are relatively few studies on the linkage between serpentinization reactions and evolution of permeability in ultramafic rocks. *MacDonald and Fyfe* [1985] performed permeability experiments on partially serpentinized intact peridotites at room temperature and obtained values in the range $l0^{-22}-10^{-21}$ m^2 for matrix permeability. *Hirose and Hayman* [2008] estimated the matrix permeability of altered ultramafic rocks and serpentinized dunite from Hole 1309D from the Integrated Ocean Drilling Program (IODP) at the AM on MAR to range between 10^{-19} and 10^{-17} m^2, suggesting that permeability was related to the presence of fractures. *Godard et al*. [2013] conducted flow-through experiments on a permeable sintered San Carlos olivine aggregate with grain size of 150–300 μm at 190°C and 19 MPa using seawater as the transporting fluid. Permeability decreased from 0.9×10^{-18} to 0.1×10^{-18} m^2 as a result of precipitation of proto-serpentine, brucite, and Fe oxides during 23 days of experiment. *Andreani et al*. [2009] investigated changes in permeability of sintered dunite samples with an average grain size of 80 μm, at confining pressure of 13 MPa and temperature of 160°C, to study the effect of in situ carbonation. Their experiments showed an increase in permeability at a rate of 0.0034 m^2/s over 8 h. *Peuble et al*. [2015] investigated carbonate mineralization during serpentinization reactions at 180°C using a sintered olivine core percolated by water enriched in CO_2. They observed localized precipitation in the flow path, indicating a control by the geometry of the porous network. They concluded that over longer time periods, a decrease in permeability could limit in situ carbonation during serpentinization reactions. None of the previous studies explored the evolution of fracture permeability during serpentinization reactions and hence do not represent the relevant fluid transport properties at mid-ocean ridges, where the permeability is controlled by fractures.

To better understand the linkages between hydraulic properties of ultramafic rocks and chemical reactions, we investigated evolution of fracture permeability (k_f) under hydrothermal conditions where the rates of serpentinization reactions are high. High-temperature flow-through experiments were performed on fractured cores of ultramafic rocks to determine an effective permeability (k_e), which represents the permeability of the sample treated as if it was homogeneous. Room temperature flow-through experiments were performed on intact disks of ultramafic rocks to determine the matrix permeability (k_m). Estimates of k_m and k_e allowed us to estimate k_f. The samples used in the experiments, described in section 2, were chosen to have different mineral assemblages and textures, to assess the role of lithology on evolution of fracture permeability. Section 3 provides details of the experimental setup. The results, presented in section 4, complement experiments on powdered and sintered samples in which the contact area between fluid and rock is large [e.g., *Godard et al*., 2013; *Malvoisin et al*., 2012]. Section 5 discusses the rates and possible mechanisms of reduction in fracture permeability and how this study helps us understand the larger permeability structure of fault zones at hydrothermal conditions. Hydrothermal circulation in ultramafic rocks encountered in some areas of oceanic crust may exhibit short-term temporal variations, reflecting the interplay between fracture sealing and fresh fracture generation that contributes to the long life of these systems.

2. Samples and Sample Preparation

2.1. Description of Samples

We used five different ultramafic rocks for these experiments (Table 1). Three, denoted by the symbols TS, JC, and ND, respectively, are dunites from the Twin Sisters Range in Washington, Jackson County in North Carolina (NC), and NewDale from the Blue Ridge province in NC. They contain approximately 85% Mg-rich

Table 1. Description of the Samples Used for the Experiments[a]

				Mineral Assemblage	
Sample	Sample ID	Locality	Average Grain Size (mm)	Major Phase ($\sim$80–90%)	Other Phases ($\sim$10–20%)
Dunite	TS	Twin Sisters, WA	0.2–5	Olivine ($Mg_{1.8}$, $Fe_{0.2}$)	Serpentine (1–2%), opx (5–10%), chromium spinel ($<$2%)
	JC	Jackson County, NC	0.1–0.3	Olivine ($Mg_{1.7}$, $Fe_{0.3}$)	Serpentine (2–4%), talc ($<$1%), actinolite/tremolite (2–5%), chlorite ($<$1%), chromium spinel (2–5%),
	ND	Spruce Pine, NC	0.1–0.6	Olivine ($Mg_{1.8}$, $Fe_{0.2}$)	Serpentine (5–8%), Talc (2%), chlorite (2%), actinolite/tremolite (2%)
Harzburgite	SQ	1.5 km southwest of San Quintin, Baja, Mexico	0.05–1	Olivine ($Mg_{1.64}$, $Fe_{0.36}$)	Serpentine ($<$1%), Opx (15%), chromium spinel (2–5%)
Pyroxenite	BC	east of Bushveld complex, South Africa	0.05–0.2	Orthopyroxene ($Mg_{1.56}$, $Fe_{0.44}$)	Serpentine (2–4%), plagioclase (2–4%), talc (2%), olivine (5%)

[a] Compositions are provided using XRD, Rigaku's PDXL software (version 1.8).

olivine, less than 10% serpentine and other minor components. One sample (SQ) is a harzburgite from near San Quintin, Baja, Mexico, with 80% Mg-rich olivine and 15% orthopyroxene, the remainder being minor minerals. The final sample (BC) is a pyroxenite from the Bushveld Complex, South Africa, containing more than 85% Mg-rich orthopyroxene, less than 10% serpentine, and other minor phases. Grain sizes of the TS and ND samples range between 0.1 and 5 mm, whereas the JC, SQ, and BC samples are more homogeneous and fine grained, with grain sizes between 0.05 and 0.2 mm. All of the samples have been partially serpentinized, ranging between 5 and 8% for ND to less than 1% for SQ. The samples selected for study do not show evidence of surficial weathering.

This suite of rock samples provides a good representation of the ultramafic rock types in the upper mantle [*Bodinier and Godard*, 2004]. Thus, these experiments can be related to serpentinization processes in many geologic settings, such as the fore-arc mantle [*Hyndman and Peacock*, 2003] and the oceanic crust [*Christensen and Salisbury*, 1975].

2.2. Sample Preparation

All samples were cored from hand-sized specimens to form cylinders with nominal diameter of 1.8 cm. After coring, samples were cut to length and end surfaces and circumferences were ground and hand polished to assure no leakage of pore fluid between the sample and outer silver jacket, as described in section 3.1. Fractured samples used in high-temperature experiments were prepared by splitting solid cylinders between steel wedges in an arbor press. These tensile fractures, split parallel to the sample axes, had well mated but rough surfaces that provided more surface area for chemical reactions than if samples had been prepared by saw cutting. Fractured samples had lengths of 2.3–2.4 cm. Samples used to determine room temperature matrix permeability were 0.9–1.3 cm in length.

3. Experimental Setup and Procedures

We performed experiments on fractured samples of ultramafic rocks using a flow-through, high-pressure, high-temperature triaxial machine. Flow results of the experiments are expressed in terms of k_e—the permeability of an equivalent, homogeneous sample with no fracture. Then, by assuming a parallel plate model for flow in a tensile fracture and independently measuring matrix permeability k_m, we calculated time-dependent changes in average fracture aperture b and fracture permeability k_f.

3.1. Fractured Samples

Sample assembly was similar to that in *Morrow et al*. [2014] (Figure 1a). Deionized water was used as the pore fluid, to minimize corrosion of the plumbing system [*Morrow et al*., 2001]. In order to reduce the degree of disequilibrium between the pore fluid and the fracture walls, a 7.5 mm thick layer of crushed ultramafic rock of the same composition as the cylindrical sample and with a grain size between 0.18 and 1.0 mm was placed upstream of the cylindrical core and within the hot zone of the furnace. Both sides of this porous layer were held in place by stainless steel screen meshes (Figure 1a). Interaction of the pore fluid with the ultramafic rock fragments in the porous layer (Figure 1b) would make the fluid chemistry more

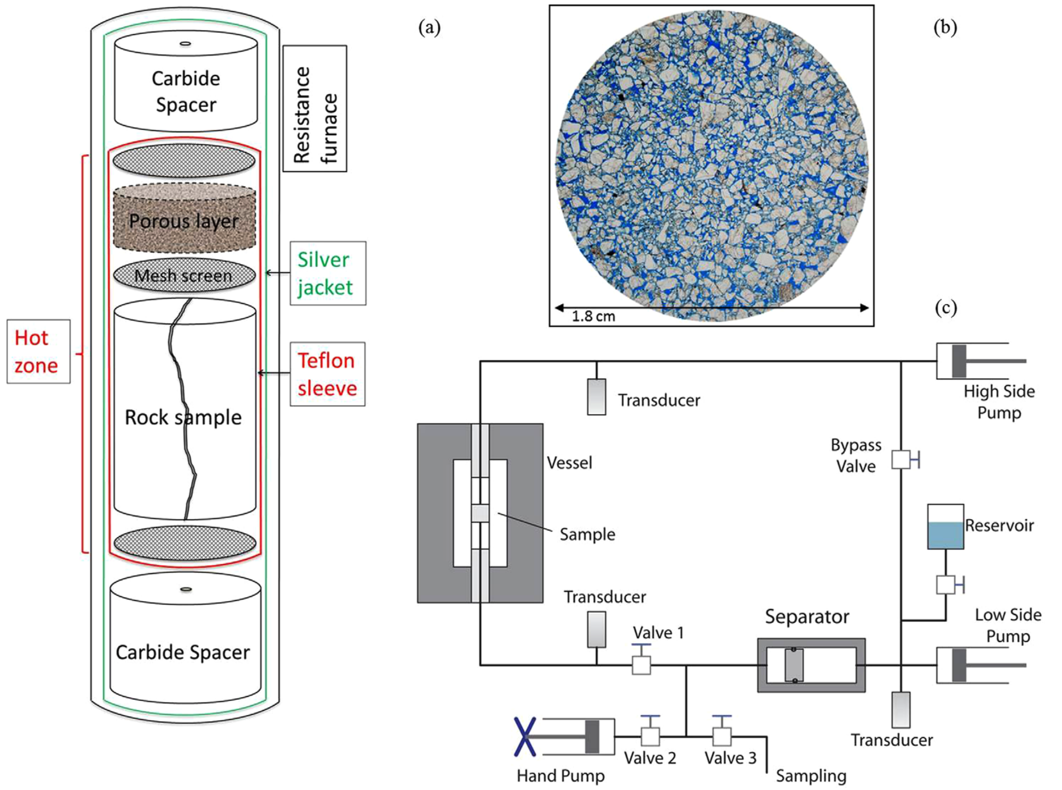

Figure 1. (a) The furnace assembly for fractured-sample experiments at elevated temperatures. (b) Cross section of the crushed-rock layer. The pore spaces are filled with blue epoxy; the porosity of the layer in all experiments is ~30%. (c) The setup of the pore pressure system. The solute-free fluid is stored in the reservoir. If the bypass valve is open, fresh water is let into the system, and the high-side pump directs the fluid to the sample.

realistic for a natural system when it entered the fractured rock core (see also *Morrow et al*. [2001]). This layer is estimated to have ~30% porosity, and it provides negligible resistance to flow (Figure 1b).

The fractured sample (D = 1.8–1.9 cm, L = 2.3–2.4 cm) and porous layer were placed in a 0.50 mm thick Teflon sleeve between carbide spacers. The whole sample assembly was housed in a 0.38 mm walled, annealed silver jacket that isolated it from the confining medium and was surrounded by a resistance furnace situated inside the pressure vessel. When confining pressure was applied, the Teflon sleeve formed an impermeable gasket between the sample and the silver jacket to prevent fluid flow along the sample surface. The upper end of the sample (Figure 1c) was connected to an external pore pressure pump and also housed a thermocouple that measured sample temperature. The lower end of the sample was connected to a second pore pressure pump and a pore fluid sampling system (Figure 1c) that was designed to extract fluid that had passed through the sample without reducing pore pressure in the sample. This is an important element of the experimental design, because the pore water in the sample is in a liquid state and a drop in pore pressure would cause it to flash to steam within the fracture. The experiments were performed at constant confining pressure (P_c) of 50 MPa and pore pressure (P_p) of 20 MPa, yielding an effective pressure ($P_{eff} = P_c - P_p$) of 30 MPa, simulating a depth of 2 km under hydrostatic fluid pressure conditions. A pore pressure difference of 2 MPa was imposed between the top and bottom pore pressure generators, although it was reached in only a few cases. Permeability measurements were possible once a measurable pore pressure difference was achieved as described in section 3.3.

3.2. Intact Samples

We performed a separate set of room temperature experiments on intact core samples (D = 1.8–1.9 cm, L = 0.9–1.3 cm) to determine matrix permeability (k_m). The methodology of the intact experiments is the same as described by *Morrow et al*. [2014], except that we use deionized water as pore fluid. Porous Berea sandstone wafers (19 mm diameter by 0.65 mm thickness) with high permeability ($>10^{-15}$ m^2) were placed on the top and bottom of the samples, to provide a uniform pore pressure to the upstream and downstream sample faces. Because the matrix permeability of Berea sandstone is many orders of magnitude higher than that of intact ultramafic rocks, it can be neglected in calculations of permeability from measured flow rates using Darcy's Law. The sample assembly was placed in a latex jacket and secured to steel end plugs.

Flow rate was measured under steady flow conditions at effective pressure (P_e) of 30 MPa and a constant pore pressure difference of 4 MPa across the sample. The matrix permeability was used in conjunction with k_e to estimate k_f and its evolution as a function of time.

3.3. Experimental Procedures

In each experiment, the sample assembly was first placed in the pressure vessel (Figure 1c) and evacuated to ensure that no air was trapped in the sample or tubing. We then applied confining and pore pressure and measured the permeability at room temperature. In the experiments on fractured samples, temperature was then raised to 260°C, which is near the temperature for peak reaction rate for serpentinization reactions [*Martin and Fyfe*, 1970]. The heating process lasted 15–20 min.

At the beginning of the experiments on fractured samples, permeability was too high for the pore pressure pump to develop a 2 MPa gradient. These samples remained under confining and pore pressure with no flow for 8–16 h between permeability tests. Then pumps were run at maximum flow rate (1.74×10^{-4} cm^3 s^{-1}) and the pore pressure drop across the sample was measured to determine permeability (supporting information). Each day $\sim$0.9 cm^3 fluid was pushed through the sample and flow rate and pore pressure were recorded every 10 s. One full stroke of the pump comprised $\sim$0.3 cm^3, and for each stroke, the collected data were averaged to provide a single permeability estimate per hour. Given the maximum flow rate of the pump, the sample dimensions and the sensitivity of the pressure transducers, the maximum permeability that can be measured at 260°C using Darcy's Law (section 4.1) is approximately 2.6×10^{-16} m^2.

To measure permeability, valve 2 and valve 3 were closed and valve 1 was open (Figure 1c), so that the pressure difference between the high and low-side pumps caused pore fluid to flow through the sample. This fluid was stored in the left side of the separator that has a free-moving internal shuttle with O-ring seals. To discharge a fluid sample, valve 1 was closed, valve 3 was opened, and the low-side pump was advanced to eject fluid stored in the separator (Figure 1c). Then the low side was brought back up to operating pressure with the hand pump, resulting in system recharge. The final fluid sample ($\sim$0.9 cm^3, comprising three full pump strokes) was diluted with 1% nitric acid to the 3 cm^3 volume that was required for analysis of major cations (Mg and Fe) and silica using an Inductively Coupled Plasma Atomic Emission Spectrometer.

Polished thin sections of the cross section of the porous layer and sections perpendicular to the fracture in the rock core were prepared after each experiment. Mineral chemistry of the reactants and precipitates was determined using a 5 nA beam current and 1 μm spot size on a Cameca SX50 Electron Microprobe (EMP) equipped with four WDS spectrometers. A Camscan Series II Scanning Electron Microscope (SEM) equipped with an upgraded image capture system and an American Nuclear Systems EDS detector was used for high-magnification examination of the samples.

4. Results

4.1. Effective Permeability of Fractured Samples

We calculated effective permeability (k_e), assuming Darcy's Law:

$$\frac{Q}{A} = -\frac{k_e}{\eta}\frac{\Delta P}{L} \tag{1}$$

where Q is the volumetric flow rate (units of m^3/s), A is the cross-sectional area of the cylinder (m^2), η is the dynamic viscosity of the fluid (Pa s), L is the sample length (m), and ΔP is the applied pore pressure difference across the sample (MPa). At 260°C and 20 MPa pore pressure, water viscosity is 9.6×10^{-5} Pa s. In equation (1), k_e denotes the permeability measured as though the flow occurs uniformly through the cross-sectional area A of the cylindrical sample. In a given experiment, A, L, and η are fixed and k_e only varies with $Q/\Delta P$. When permeability is high, Q is limited to the maximum pump flow rate and permeability changes

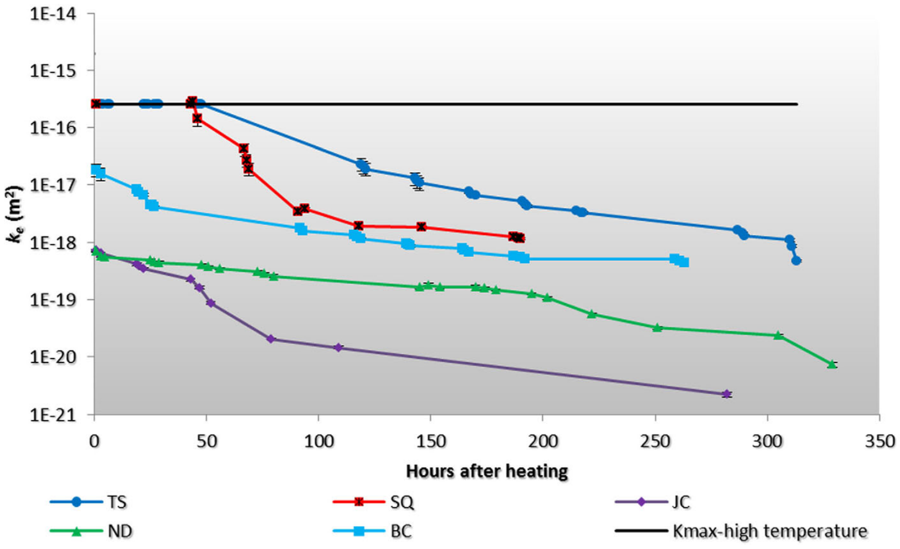

Figure 2. Evolution of effective permeability k_e of the fractured sample, where k_e is calculated assuming that flow is distributed across the cross-sectional area of the cylinders. Time = 0 is when the sample reached 260°C. Each measurement is averaged over the time it takes for a full stroke of the high-side pump, which is 0.3 cm^3. The black line represents maximum measurable permeability at 260°. The upward-pointing arrows indicate permeabilities that are at or above the maximum measurable limit.

are reflected by changes in ΔP. For low permeability, a constant pressure difference of 2 MPa is maintained by computer control and permeability changes are reflected by changes in Q.

Evolution of k_e during the high-temperature experiments is shown in Figure 2. The time $t = 0$ is the time at which the sample reached 260°C. All of the samples showed at least 2 orders of magnitude drop in effective permeability in the 200–330 h of the experiments. The initial high temperature values of k_e ranged from 10^{-18} to more than 10^{-16} m^2 and were somewhat variable, because starting permeability was sensitive to how well the two sample halves were mated, which could be influenced by grain size and degree of alteration [*Morrow et al.*, 2001]. The TS and SQ samples have significantly larger maximum grain size, smaller amounts of alteration, and thus more fracture surface roughness that resulted in poor mating of the sample halves and higher initial permeability than BC, JC, and ND (Table 1). The initial permeability of samples TS and SQ at 260°C exceeded the maximum measurable value for the experimental system but decreased into the measurable range after about 50 h. The final values of k_e ranged between 10^{-18} and 10^{-20} m^2, which is similar to the estimated permeabilities of partially serpentinized peridotites [*MacDonald and Fyfe*, 1985; *Hirose and Hayman*, 2008; *Godard et al.*, 2013; *Tenthorey et al.*, 2003].

Table 2. Estimates of Matrix Permeability (k_m) at Room Temperature and Fracture Permeability (*kf*) and Aperture (*b*) Near the Beginning and at the End of the High-Temperature Experiments

	23°C		260°C	
Sample	k_m (m^2 × 10^{-23})	Time (h)	k_f^a (m^2 × 10^{-16})	b (m × 10^{-6})
TS	3.12	119	2070	1.58
		313	155	0.43
SQ		46	6870	2.90
		189	281	0.58
JC	3.14	1	206	0.50
		282	4.2	0.07
ND	20.30	1	201	0.50
		329	9.2	0.10
BC	4.61	1	1770	1.46
		263	146	0.42

^{a}Estimates for TS, JC, ND, and BC are calculated using equation (4) and for SQ using equation (5).

Factors contributing to uncertainty in determining k_e stem from many causes, including sample dimensions as the ratio *L/A* in equation (1), which contributes less than 0.5% to uncertainty. Pore pressure precision is 0.005 MPa and for a 2 MPa pressure drop across the sample contributes 0.25% uncertainty to the permeability determination. For sample permeability above about 10^{-17} m^2, the pore pressure generator cannot maintain the desired 2 MPa pressure gradient. For permeability below about 10^{-17} m^2, measurement of flow rate Q dominates the uncertainty in determining permeability. For the range $10^{-20} < k < 10^{-17}$ m^2, uncertainty in Q, and therefore k, is less than $\pm 5\%$. For $k < 10^{-20}$ m^2, individual flow tests may take many hours to days and room temperature fluctuations degrade the flow rate determination so that uncertainty in k can increase to $\pm 10\%$ [*Morrow et al.*, 2014].

4.2. Permeability of Intact Samples

Permeability of a set of intact samples was determined using equation (1) where k is now matrix permeability, k_m. All tests were performed at 23°C and effective confining pressure of 30 MPa. Table 2 shows the measured values of k_m. The SQ sample contained a preexisting fracture that made permeability measurements unrepresentative of matrix properties.

4.3. Evolution of Fracture Permeability

The effective permeability of the cylindrical samples with a through-going fracture can be treated in terms of layers of different permeability parallel to the flow direction (Figure 1a). Then k_e of the sample calculated from equation (1) can be written as:

$$k_e = \frac{k_m A_m + k_f A_f}{A_m + A_f} \tag{2}$$

where k_f is fracture permeability, $A_f = 2rb$ m^2 is the fracture cross-sectional area where r is the radius of the sample and b is the average fracture aperture m, and the total sample cross-sectional area is $A_m + A_f = \pi r^2$ m^2.

Although the fractures generated in the core samples may exhibit significant aperture variations and tortuosity along the flow path, we assume that k_f can be approximated using the cubic law for flow in a fracture represented by parallel plates [*Bear*, 1972; *Witherspoon et al.*, 1980]:

$$k_f = \frac{b^2}{12} \tag{3}$$

By inserting equation (3) into equation (2), one obtains:

$$k_e = \frac{k_m(\pi r^2 - 2rb) + \frac{b^2}{12}(2rb)}{\pi r^2} \tag{4}$$

The estimated average fracture aperture, b, at the beginning and end of the heated tests was calculated using equation (4) and the measured values of k_e and k_m (Table 2). b for all the samples ranges from 0.01 to 1 μm (Table 2) and over the course of each high-temperature experiment, it decreases by as much as an order of magnitude.

To investigate evolution of fracture permeability, we substitute the calculated values of b into equation (3) to determine k_f both at room temperature and as a function of time at 260°C (Table 2). Compared with the evolution of k_e in Figure 2, k_f follows the same trend but is approximately 3–6 orders of magnitude greater than k_e and approximately 9 orders of magnitude higher than k_m. These differences indicate that fluid flow in the matrix is negligible and equation (4) can be simplified to:

$$k_e \cong \frac{b^3}{6\pi r} = \frac{2bk_f}{\pi r} \tag{5}$$

Equations (3) and (5) show that for individual experiments, $b \propto {k_e}^{1/3}$ and consequently $k_f \propto {k_e}^{2/3}$. For the SQ sample, we were unable to determine k_m by direct measurement. In this case, we used equation (5) to determine k_f (Figure 4) and b (Table 2).

Note that in equations (2) and (4), we use the measured room temperature value of k_m at $P = 30$ MPa, even though its value at 260°C may change as a result of thermal cracking or mineral deformation [e.g., *Moore et al.*, 1994]. Calculated k_f is so much greater than k_m that, even though the fracture accounts for less than 0.02% of the cross-sectional area of sample, flow in the fracture still dominates flow in the rock matrix. Reynolds number for flow focused in a fracture can be estimated using $Re = \rho v b/\eta$ where ρ is density of (10^3 kg/m^3), $v = Q/A$ is velocity of pore fluid in the fracture ($A = bd$) that ranges between $3 \times 10^{-3} - 2 \times 10^{-2}$ (m/s), and η is the viscosity of water at 260°C (9.6×10^{-5} Pa s). The values of Re fall in the range of $10^{-3} - 10^{-1}$, which is considerably smaller than 10 and indicates laminar flow in the fracture [e.g., *Zimmerman et al*., 2004].

Table 3. The Chemical Composition of Newly Precipitated Material in the Fracture From Microprobe Analysis

Sample	TS	SQ	JC	ND	BC
SiO_2	39.76	37.71	41.00	39.12	37.79
MgO	37.05	33.29	39.92	38.59	17.95
FeO	5.97	8.00	3.43	4.34	26.01
Al_2O_3	0.25	1.45	0.06	0.02	2.79
TiO_2	0.02	0.13	0.01	0.00	0.12
Cr_2O_3	0.09	0.05	0.02	0.03	0.13
CaO	0.10	0.71	0.05	0.04	0.63
Total	83.24	81.34	84.48	82.15	85.42
Mg/(Mg + Fe)	0.92	0.88	0.96	0.94	0.59
Serpentine composition	$(Mg, Fe, Al^{VI}, Ti, Cr, Ca)_6 (Si, Al^{IV})_4 O_{10} (OH)_8$				

4.4. Rock Mineralogy and Fluid Chemistry Data

The Back-Scattered Electron (BSE) images collected using SEM (Figure 4) show needle-shaped crystals precipitated along the walls of the fracture and on the surfaces of loose grains that may have moved along the fracture during flow. In all of the samples, more than 50% of the length of the tensile fracture has new precipitation (Figures 4a and 4b) and about 10% of the fracture length is blocked with loose grains (Figure 4c). Minor amounts of old serpentine phases were observed along the walls of the tensile fracture, which could result in the reduction of the available reactive surface area.

The EMP analyses revealed that alteration products are mainly rich in SiO_2, MgO, and FeO, and the compositions are consistent with the mineral serpentine (Table 3). The Mg/(Mg+Fe) ratio of the newly precipitated serpentine in all peridotite samples is 0.9. In a comparison between the composition of the newly precipitated serpentine and old serpentine, SiO_2 contents are 0.1–6.7% higher in the newly precipitated serpentine. The concentrations of SiO_2 and MgO of precipitates in the TS, JC, and ND dunite samples are higher than those in the SQ sample. The FeO contents of the serpentine deposits in all peridotite samples are less than 10 wt %, and the concentrations of Al_2O_3, TiO_2, Cr_2O_3, and CaO are less than $\sim$3 wt %. The high Fe contents of the serpentine from the BC pyroxenite may indicate precipitation of serpentine accompanied by a Fe-rich phase. Most of the new precipitates in all of the samples lined the wall of the tensile fracture; negligible amounts of precipitated material were detected in the intergranular pores of the layers of crushed rock above the samples. There is no evidence of brucite precipitation in any of the samples. A similar result has been observed previously by *Okamoto et al*. [2011], where continuous supply of fresh fluid causes the serpentinization reactions to proceed without the formation of brucite. *Klein et al*. [2015] also did not observe brucite in their experiments, as a result of simultaneous dissolution of olivine and orthopyroxene.

The ideal case for fluid sampling and analysis would be that a 2 MPa pore pressure gradient is maintained across the sample cell, allowing for slow, continuous flow. However, as described previously (section 3.3), for most of the experiments, the 2 MPa pore pressure gradient was not reached. The total fluid volume contained in the porous layer (assuming $\sim$30% porosity) plus the fracture (assuming the average estimated aperture from Table 2) was calculated to be $\leq$0.6 cm^3. Given that the volume of each fluid sample collected is $\sim$0.9 cm^3, the first fluid samples contain a considerable proportion of essentially unreacted deionized water that was rapidly flushed through the system. As permeability decreases, the amount of time required for an increment of fluid to traverse the fracture increases. The final fluid sample collected during an experiment therefore comes closest to equilibration with the rock sample. Concentrations of Mg, Fe, Si, Na, Ca, and Al increased from zero in initial deionized water to $10^{-5}-10^{-3}$ molar in the final pore fluid sample. The overall trend of fluid chemistry exhibits significant increases in the key chemical constituents of serpentinization reactions that are consistent with dissolution of ultramafic rocks at high temperature. The fluid chemistry data (provided in *Farough* [2015]) are only used as evidence that water-rock reactions occurred. More detailed analysis of fluid chemistry is out of the scope of this paper.

5. Discussion

5.1. Rate of Reduction of Fracture Permeability With Time

The reduction in fracture permeability with time can be approximated by an exponential function:

$$k_f = k_{f0} e^{\left(-\frac{t}{t^*}\right)} \tag{6}$$

where k_{f0} is the starting permeability of the modeled interval and t^* is the characteristic decay time of the best fit exponential function in hours. Figure 3 shows the results. During the first 25–91 h of the

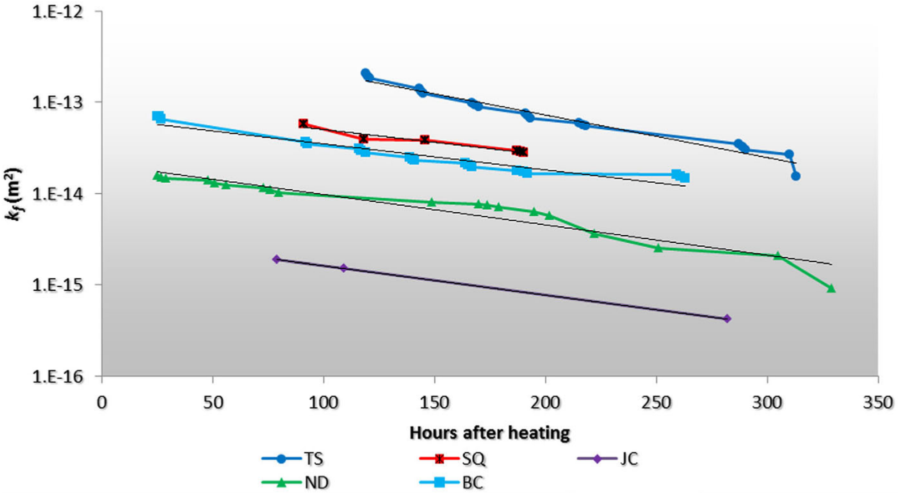

Figure 3. Fitted exponential functions to estimated k_f values presented in Table 2.

experiments, samples SQ, BC, and JC depict a rapid decrease in permeability. Sample ND shows a less significant slope change in the first 25 h of the experiment (see Figure 2). This early rapid reduction in permeability likely represents the effect of dissolution of asperities. Our interpretation is that following disappearance of asperities, mineral precipitation becomes the controlling factor on permeability reduction. In samples TS, ND, and BC, a second slope change is observed at the very end of the experiments (see Figure 2) which can be interpreted as blockage of critical necks as a result of mineral precipitation, but based on these short-term data, we cannot determine if the decrease will continue or not. The characteristic decay time as a result of mineral precipitation t^* varies by approximately a factor of 2, ranging between approximately 91 and 167 h (Table 4). There is no apparent relationship between lithology and t^* in the experiments.

Previous laboratory studies on the evolution of permeability in both intact and fractured granitic rocks [*Moore et al*., 1994; *Morrow et al*., 2001] also showed that the rate of permeability decrease fits an exponential function after a rapid initial decline in permeability. The experiments of *Morrow et al*. [2001] on fractured samples of granite at 150 and 250°C at 150 MPa confining pressure and 100 MPa pore pressure exhibited characteristic decay times between approximately 730 and 1580 h. Notably, the decay times for the ultramafic rocks are all significantly shorter than for the granitic rocks under generally similar *P-T* conditions. The difference in decay times for ultramafic and granitic rocks suggests that the rate of reaction in ultramafic rocks is faster than that in granitic rocks under these experimental conditions.

5.2. Mechanisms of Reduction in Fracture Permeability

The changes in permeability and aperture of a natural, rough-walled fracture during flow under hydrothermal conditions can be affected by several factors. The most important and effective among these are mineral dissolution and precipitation along the walls of the fracture, pressure solution of contacting asperities, transport of fine-grained solids along the flow path, and thermal cracking and fracture morphology. Mineral dissolution at free faces of the fracture and thermal cracking act to increase permeability, whereas mineral precipitation and pressure solution of contacting asperities act to decrease permeability. Transport of fine grains and tortuosity of the flow path can affect permeability in various ways. For example, blockage of the flow path with loose mineral grains (Figure 4c) acts to reduce permeability and increase tortuosity, whereas dissolution or breakage of the blocked grains has the opposite effect. Pressure solution of contacting asperities, as a consequence of confining pressure, governs the rate of aperture change, especially in the early stages of the experiments [*Lang et al*., 2015; *Moore et al*., 1994]. The SEM images (Figures 4a–4c) show that precipitation of minerals and blockage of the flow path with loose grains also contributed to the sealing process. A comparison between estimated average aperture, b, in Table 2 and observed aperture in Figures 4a–4c (~2 to 6 μm) suggests that the spatial arrangement of the aperture distribution is strongly heterogeneous. The equal height of the precipitates in Figures 4a and 4b suggests that the width of the fracture was spanned with precipitates, and that after the confining pressure was removed and/or during sectioning of the samples, the fracture reopened.

The parallel plate law used to estimate average aperture assumes that the tortuosity of the flow path is negligible and that fracture roughness can be described as though all the flow is parallel to the pressure gradient [e.g., *Tsang*, 1984]. In a rough-walled fracture under confining pressure, however, portions of the fracture may be closed as a result of mineral dissolution and precipitation reactions, leading to a reduction in fracture aperture and an increase in tortuosity of the flow path. As the tortuosity increases, the effective fracture permeability may be significantly smaller than given by the cubic law [*Tsang*, 1984].

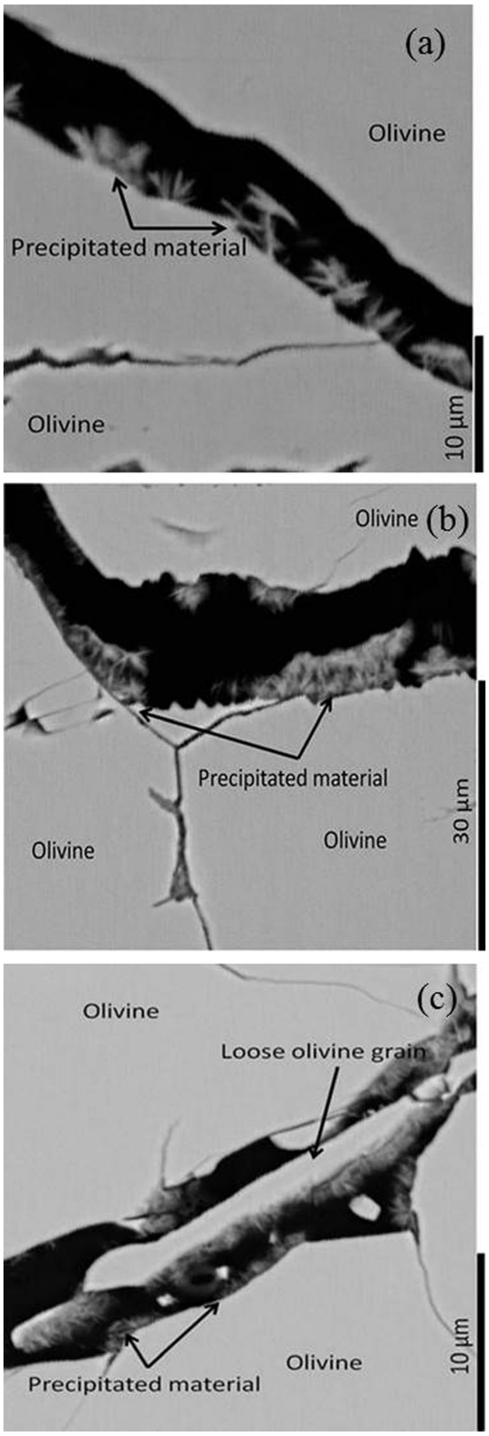

Figure 4. BSE images of the tensile fracture. (a and b) Needle-shaped crystals precipitated along the wall of the fracture. (c) Precipitation of needle-shaped crystals along the walls of the fracture and along the sides of a loose grain.

5.3. Implications for Mid-Ocean Ridge Hydrothermal Systems

The goal of this study was to better understand the processes controlling hydraulic properties of the host rock during serpentinization reactions in ultramafic-hosted hydrothermal systems in oceanic crust, given that flow is primarily controlled by fractures. We understand the limitations of applying a 2 week long study of a single fracture with an aperture on the scale of microns to a complicated network of natural fractures encompassing a range of sizes that were subjected to tens to hundreds of years of fluid circulation. Nevertheless, extrapolating our results (Figure 3) to longer times suggests that the permeability of a fracture $\sim 10^{-6}$ m in width would decay to $k_f \sim 10^{-23}$ m^2 in approximately 2–4 months, resulting in fracture permeability approximately equal to matrix permeability. On this basis, mechanisms to open new surface area to fluid flow must occur to maintain the hydrothermal circulation in ultramafic rocks in seafloor hydrothermal systems. Factors such as tectonic activity [*Andreani et al.*, 2009] and crystallization pressure [e.g., *Andreani et al.*, 2007; *Kelemen and Hirth*, 2012] coupled with mineral precipitation may result in complex time-dependent cyclic behavior of fluid circulation in the oceanic crust, with impermeable mineral seals neighboring high-permeability areas.

Although permeability decreased rapidly as a function of time in these experiments, Figure 4c shows short, thin fractures that appear to have extended away from etch pits. If experiments were run for greater durations, these small fractures might eventually contribute to a secondary fracture network, thereby generating new permeability [e.g., *Malvoisin et al.*, 2012; *Kelemen and Hirth*, 2012]. Some analyses of mineralized fractures in IODP samples indicate different generations of fractures in fracture networks [*Beard et al.*, 2009].

Fluid circulation in seafloor hydrothermal systems is fed by a large system of fractures that are continually plugging and fracturing in different places. These processes likely create a heterogeneous permeability

Table 4. The Intercept (k_{f0}), Characteristic Decay Time (t^*), and Ratio of Standard Error (STD Error) to the Estimated Value for k_{f0} and t^*, and R^2 Values of Fitted Exponential Equations for the Fracture Permeability (k_f) Estimates

	Time (h)	k_{f0} ($m^2 \times 10^{-14}$)	STD Error k_{f0}/k_{f0}	t^* (h)	STD Error t^*/t^*	R^2
TS	119–310	60	0.004	91	0.046	0.96
SQ	91–189	10	0.015	167	0.168	0.93
JC	79–282	7	0.005	143	0.122	0.91
ND	25–305	2	0.002	125	0.063	0.91
BC	25–259	0.3	0.003	143	0.076	1

structure in oceanic crust, which could affect the behavior or the life cycle of seafloor hydrothermal systems.

6. Conclusions

This study monitors changes in permeability of fractured samples of ultramafic rocks under hydrothermal conditions, in order to better understand the rate at which serpentinization reactions affect fracture permeability and to shed some light on the linkages between the physical and chemical changes of the oceanic crust during hydrothermal circulation in ultramafic rocks. For a variety of rock lithologies, the experimental results show that fracture permeability decreased as much as 2 orders of magnitude during the 200–330 h of the high-temperature experiments.

Although several factors may have contributed to the decrease in permeability, precipitation of serpentine minerals along the walls of the tensile fracture played an important role. These results suggest that serpentinization reactions can block flow paths and impede fluid circulation in the oceanic crust in a relatively short time, even with the limited reactive surface area available in fractures. Long-term maintenance of fluid circulation in ultramafic-hosted hydrothermal systems requires the frequent generation of new permeable pathways, perhaps by a combination of tectonic activity and crystallization pressure.

Acknowledgments
We thank the Editor Thorsten Becker, an anonymous reviewer, and Marguerite Godard, C. Neuzil, J. Taron, and M. Diggles for their constructive reviews on an earlier version of this manuscript. The authors thank Neil Johnson for XRD assistance and sample collection and Luca Fedele for EMP and SEM assistance. Edmond A. Mathez and the American Museum of Natural History, NY, provided some of the samples. Lee-Grey Boze helped with the sample preparation and collection of intact permeability data. The authors also would like to thank J. Donald Rimstidt, James Beard, and Esther Schwarzenbach for useful conversations regarding serpentinization processes and data interpretation. This work was partially supported by NSF grant OCE1131471 to R.P.L. All data used in this paper can be found in the tables and have been properly cited. Any use of trade, firm, or product names is for descriptive purposes only and does not imply endorsement by the U.S. Government.

References

Aharonov, E., E. Tenthorey, and C. H. Scholz (1998), Precipitation sealing and diagenesis: 2. Theoretical analysis, *J. Geophys. Res.*, *103*(B10), 23,969-23,981.

Andreani, M., C. Mével, A. M. Boullier, and J. Escartín (2007), Dynamic control on serpentine crystallization in veins: Constraints on hydration processes in oceanic peridotites, *Geochem. Geophys. Geosyst.*, *8*, Q02012, doi:10.1029/2006GC001373.

Andreani, M., L. Luquot, P. Gouze, M. Godard, E. Hoise, and B. Gibert (2009), Experimental study of carbon sequestration reactions controlled by the percolation of CO_2-rich brine through peridotites, *Environ. Sci. Technol.*, *43*(4), 1226–1231.

Bach, W., N. R. Banerjee, H. J. Dick, and E. T. Baker (2002), Discovery of ancient and active hydrothermal systems along the ultra-slow spreading Southwest Indian Ridge 10°–16°E, *Geochem. Geophys. Geosyst.*, *3*(7), doi:10.1029/2001GC000279.

Batuyev, B. N., A. G. Krotov, V. F. Markov, G. A. Cherkashev, S. G. Krasnov, and Y. D. Lisitsyn (1994), Massive sulfide deposits discovered and sampled at 14°45′N, Mid-Atlantic Ridge, *BRIDGE Newsl.*, *6*, 6–10.

Bear, J. (1972), *Dynamics of Fluids in Porous Media*, 764 pp., Elsevier, N. Y.

Beard, J. S., B. R. Frost, P. Fryer, A. McCaig, R. Searle, B. Ildefonse, P. Zinin, and S. K. Sharma (2009), Onset and progression of serpentinization and magnetite formation in olivine-rich troctolite from IODP Hole U1309D, *J. Petrol.*, *50*(3), 387–403.

Bodinier, J., and M. Godard (2004), *Treatise on Geochemistry, vol. 2, The Mantle and Core*, pp. 103–170, Elsevier, Amsterdam.

Bogdanov, Y. A., A. M. Sagalevitch, E. S. Chernyaev, A. M. Ashadze, E. G. Gurvich, V. N. Lukashin, G. V. Ivanov, and V. N. Peresypkin (1995), A study of the hydrothermal field at 14°45′N on the Mid-Atlantic Ridge using the "Mir" submersibles, *BRIDGE Newsl.*, *9*, 9–13.

Cann, J., D. Blackman, D. Smith, E. McAllister, B. Janssen, S. Mello, E. Avgerinos, A. Pascoe, and J. Escartin (1997), Corrugated slip surfaces formed at ridge-transform intersections on the Mid-Atlantic Ridge, *Nature*, *385*(6614), 329–332.

Cannat, M. (1993), Emplacement of mantle rocks in the seafloor at mid-ocean ridges, *J. Geophys. Res.*, *98*(B3), 4163–4172.

Carlson, R. (2001), The abundance of ultramafic rocks in Atlantic Ocean crust, *Geophys. J. Int.*, *144*(1), 37–48.

Charlou, J. L., J. P. Donval, Y. Fouquet, P. Jean-Baptiste, and N. Holm (2002), Geochemistry of high H_2 and CH_4 vent fluids issuing from ultramafic rocks at the Rainbow hydrothermal field (36°14′ N, MAR), *Chem. Geol.*, *191*, 345–359.

Christensen, N. I., and M. H. Salisbury (1975), Structure and constitution of the lower oceanic crust, *Rev. Geophys.*, *13*(1), 57–86.

Coleman, R. G. (1971), Petrologic and geophysical nature of serpentinites, *Geol. Soc. Am. Bull.*, *82*(4), 897–918.

Connelly, D. P., J. T. Copley, B. J. Murton, K. Stansfield, P. A. Tyler, C. R. German, and S. Wilcox (2012), Hydrothermal vent fields and chemosynthetic biota on the world's deepest seafloor spreading centre, *Nat. Commun.*, *3*, 620.

Escartin, J., M. Cannat, G. Pouliquen, A. Rabain, and J. Lin (2001), Crustal thickness of V-shaped ridges south of the Azores: Interaction of the Mid-Atlantic Ridge (36°- 39°N) and the Azores hot spot, *J. Geophys. Res.*, *106*(B10), 21,719-21,736.

Evans, J. P., C. B. Forster, and J. V. Goddard (1997), Permeability of fault-related rocks, and implications for hydraulic structure of fault zones, *J. Struct. Geol.*, *19*(11), 1393–1404.

Farough, A. (2015), An experimental study on characterization of physical properties of ultramafic rocks and controls on evolution of fracture permeability during serpentinization at hydrothermal conditions, PhD dissertation, 95 pp., Va. Tech, Blacksburg.

Früh-Green, G. L., D. S. Kelley, S. M. Bernasconi, J. A. Karson, K. A. Ludwig, D. A. Butterfield, C. Boschi, and G. Proskurowski (2003), 30,000 years of hydrothermal activity at the Lost City vent field, *Science*, *301*(5632), 495–498.

Godard, M., L. Luquot, M. Andreani, and P. Gouze (2013), Incipient hydration of mantle lithosphere at ridges: A reactive-percolation experiment, *Earth Planet. Sci. Lett.*, *371*, 92–102.

Hirose, T., and N. Hayman (2008), Structure, permeability, and strength of a fault zone in the footwall of an oceanic core complex, the Central Dome of the Atlantis Massif, Mid-Atlantic Ridge, 30°N, *J. Struct. Geol.*, *30*, 1060–1071.

Hyndman, R. D., and S. M. Peacock (2003), Serpentinization of the forearc mantle, *Earth Planet. Sci. Lett.*, *212*(3-4), 417–432.

Karner, S. L., C. Marone, and B. Evans (1997), Laboratory study of fault healing and lithification in simulated fault gouge under hydrothermal conditions, *Tectonophysics*, *277*, 41–55.

Kelemen, P. B., and G. Hirth (2012), Reaction-driven cracking during retrograde metamorphism: Olivine hydration and carbonation, *Earth Planet. Sci. Lett.*, *345*, 81–89.

Kelley, D. S., J. A. Karson, D. K. Blackman, G. L. Früh-Green, D. A. Butterfield, M. D. Lilley, and P. Rivizzigno (2001), An off-axis hydrothermal vent field near the Mid-Atlantic Ridge at 30 N, *Nature*, *412*(6843), 145–149.

Klein, F., N. G. Grozeva, J. S. Seewald, T. M. McCollom, S. E. Humphris, B. Moskowitz, T. S. Berquo, and W.-A. Kahl (2015), Experimental constraints on fluid-rock reactions during incipient serpentinization of harzburgite, *Am. Mineral.*, *100*(4), 991–1002.

Lang, P. S., A. Paluszny, and R. W. Zimmerman (2015), Hydraulic sealing due to pressure solution contact zone growth in siliciclastic rock fractures, *J. Geophys. Res. Solid Earth*, *120*, 4080–4101, doi:10.1002/2015JB011968.

Lowell, R. P., A. Farough, J. Hoover, and K. Cummings (2013), Characteristics of magma-driven hydrothermal systems at oceanic spreading centers, *Geochem. Geophys. Geosyst.*, *14*, 1756–1770, doi:10.1002/ggge.20109.

Macdonald, A., and W. Fyfe (1985), Rate of serpentinization in seafloor environments, *Tectonophysics*, *116*(1), 123–135.

Malvoisin, B., F. Brunet, J. Carlut, S. Rouméjon, and M. Cannat (2012), Serpentinization of oceanic peridotites: 2. Kinetics and processes of San Carlos olivine hydrothermal alteration, *J. Geophys. Res.*, *117*, B04102, doi:10.1029/2011JB008842.

Martin, B., and W. Fyfe (1970), Some experimental and theoretical observations on the kinetics of hydration reactions with particular reference to serpentinization, *Chem. Geol.*, *6*, 185–202.

Moore, D. E., D. A. Lockner, and J. D. Byerlee (1994), Reduction of permeability in granite at elevated temperatures, *Science*, *265*(5178), 1558–1561.

Morrow, C. A., D. E. Moore, and D. A. Lockner (2001), Permeability reduction in granite under hydrothermal conditions, *J. Geophys. Res.*, *106*(B12), 30,551-30,560.

Morrow, C. A., D. A. Lockner, D. E. Moore, and S. Hickman (2014), Deep permeability of the San Andreas Fault from San Andreas Fault Observatory at Depth (SAFOD) core samples, *J. Struct. Geol.*, *64*, 99–114.

Nakatani, M. (1998), A new mechanism of slip weakening and strength recovery of friction associated with the mechanical consolidation of gouge, *J. Geophys. Res.*, *103*(B11), 27,239-27,256.

O'Hanley, D. S. (1992), Solution to the volume problem in serpentinization, *Geology*, *20*(8), 705–708.

Okamoto, A., Y. Ogasawara, Y. Ogawa, and N. Tsuchiya (2011), Progress of hydration reactions in olivine–H_2O and orthopyroxenite–H_2O systems at 250˚C and vapor-saturated pressure, *Chem. Geol.*, *289*(3–4), 245–255.

Olsen, M. P., C. H. Scholz, and A. Léger (1998), Healing and sealing of a simulated fault gouge under hydrothermal conditions: Implications for fault healing, *J. Geophys. Res.*, *103*(B4), 7421–7430.

Peuble, S., M. Godard, L. Luquot, M. Andreani, I. Martinez, and P. Gouze (2015), CO_2 geological storage in olivine rich basaltic aquifers: New insights from reactive-percolation experiments, *Appl. Geochem.*, *52*, 174–190.

Plümper, O., A. Royne, A. Magraso, and B. Jamtveit (2012), The interface-scale mechanism of reaction-induced fracturing during serpentinization, *Geology*, *40*(12), 1103–1106.

Polak, A., D. Elsworth, H. Yasuhara, A. Grader, and P. Halleck (2003), Permeability reduction of a natural fracture under net dissolution by hydrothermal fluids, *Geophys. Res. Lett.*, *30*(20), 2020, doi:10.1029/2003GL017575.

Tenthorey, E., C. H. Scholz, E. Aharonov, and A. Léger (1998), Precipitation sealing and diagenesis: 1. Experimental results, *J. Geophys. Res.*, *103*(B10), 23,951-23,967.

Tenthorey, E., S. F. Cox, and H. F. Todd (2003), Evolution of strength recovery and permeability during fluid–rock reaction in experimental fault zones, *Earth Planet. Sci. Lett.*, *206*(1), 161–172.

Tsang, Y. (1984), The effect of tortuosity on fluid flow through a single fracture, *Water Resour. Res.*, *20*(9), 1209–1215.

Witherspoon, P. A., J. S. Y. Yang, K. Iwari and J. E. Gale (1980), Validity of cubic law for fluid flow in a deformable rock fracture, *Water Resour. J.*, *16*, 1016–1024.

Zimmerman, R. W., A. Al-Yaarubi, C. C. Pain, and C. A. Grattoni (2004), Non-linear regimes of fluid flow in rock fractures, *Int. J. Rock Mech. Min. Sci.*, *41*, doi:10.1016/j.ijmms2003.12.045.